

Thermal properties of Dirac fermions in Xenes: Model studies

Friedhelm Bechstedt,¹ Simone Grillo²,³ Olivia Pulci,³ and Paola Gori⁴

¹*Institut für Festkörperteorie und -optik, Friedrich-Schiller-Universität Jena, Max-Wien-Platz 1, 07743 Jena, Germany*

²*Dipartimento di Fisica, Università di Roma “Tor Vergata,” Via della Ricerca Scientifica 1, 00133 Roma, Italy*

³*INFN, Via della Ricerca Scientifica 1, 00133 Roma, Italy*

⁴*Dipartimento di Ingegneria Industriale, Elettronica e Meccanica, Università “Roma Tre,” Via della Vasca Navale 79, 00146 Roma, Italy*



(Received 19 August 2021; revised 7 October 2021; accepted 11 October 2021; published 25 October 2021)

The thermal properties and the electrical conductance are studied for 2D electron gases in doped Xenes – graphene, silicene, germanene, stanene, and plumbene – applying a four-band model to describe the low-energy Dirac-fermion-like electronic excitations. Spin-orbit interactions to discriminate the five Xenes and the influence of an electric field in the normal direction, are taken into account. The density of states and the spectral behavior of the current-current correlation function allow the calculation of the Onsager coefficients. They give analytical formulas for the electronic contributions to the heat capacity and thermal conductance. Also, the electrical conductance can be described within the same framework, if the scattering properties of the electron gases are simulated by constant broadening parameters. For all these thermal and transport properties, only a weak variation with the Xene is found, because of their small spin-orbit-induced gaps, with the exception of plumbene. The heat capacity of Xenes does not show a Schottky anomaly. The thermal conductance increases linearly or quadratically with temperature depending on the temperature range. A similar behavior characterizes the electrical conductance. The dominance of Dirac fermions, i.e., linear bands, determines the ratio of electron thermal conductance and electric conductance, which depends on doping level and temperature. It violates the Wiedemann-Franz law known for 3D electron gases with parabolic energy-momentum dispersion. The Lorenz number is generally much larger for 2D electron gases with almost Dirac character of the dispersion relation.

DOI: [10.1103/PhysRevB.104.165420](https://doi.org/10.1103/PhysRevB.104.165420)

I. INTRODUCTION

Research on two-dimensional (2D) materials is driven both by fundamental interest and the perspective of applications in novel devices. Among the 2D systems, atomic monolayer structures exhibit outstanding electronic, optical, transport but also thermal properties because of strong quantum size effects and formation of a quantum spin Hall phase. Elemental monolayers consisting of group-IV atoms carbon (C), silicon (Si), germanium (Ge), tin (Sn), and lead (Pb) and crystallizing in a hexagonal honeycomb geometry, the so-called Xenes graphene, silicene, germanene, stanene, and plumbene [1], are of special interest. For instance, the unbuckled graphene layer with zero gap exhibits amazing physical effects such as a constant infrared absorbance ruled by the fine-structure constant [2], the room temperature quantum Hall effect [3], a high intrinsic carrier mobility [4], and a large thermal conductivity [5].

The Si, Ge, Sn, and Pb counterparts of graphene cannot be produced by exfoliation techniques but have been fabricated on various substrates in the last years [1]. Theoretically, as freestanding low-buckled honeycomb layers [6], their low-energy electronic excitations are dominated by Dirac fermions. However, due to the increasing spin-orbit coupling (SOC) along the column C → Si → Ge → Sn → Pb in the Periodic table, the linear bands near the K and K' corner points of the hexagonal Brillouin zone (BZ) are modified. The

SOC-induced gap opening leads to massive Dirac particles [7]. Above this gap, a constant infrared optical absorbance as in graphene is predicted also for the other Xenes [7,8]. The Xenes are promising candidates for application in ultrafast detectors, ultra-low-power spintronics, and quantum devices [9–11]. The gap opening, at least in germanene and stanene with stronger SOC, makes these materials suitable to room-temperature quantum spin Hall (QSH) insulators [12,13], although the quantization of the spin Hall conductivity may be slightly destroyed by the Rashba contribution to the SOC [14,15]. Interestingly, pristine plumbene is a trivial insulator, not showing the topological properties of the other Xenes [16].

Besides electric conduction, thermal conduction is another important mechanism of energy or information transport [17]. It is mediated by either electrons or phonons. Thermal transport in Xenes has been essentially investigated as driven by lattice vibrations, in agreement with their dominance over the electronic contribution in graphene [18]. Phonon transport in silicene and germanene, but also stanene or plumbene, has been studied within *ab initio* theoretical approaches [19–24]. Applying the Green-Kubo method or molecular dynamics investigations, thermal conductivities of silicene vibrational lattice in the range of 5–65 W/mK have been predicted [25–28].

Graphene has a significantly higher phonon thermal conductance than its electronic counterpart at room temperature [5,18,29–31]. This fact is in complete contrast to metals,

where the electronic contribution dominates the thermal properties [32]. In the case of the other Xenes with layer buckling – silicene, germanene, stanene, and plumbene – the situation is less clear. Model studies on the electronic contribution to the thermal properties have been performed without taking SOC into account [33,34] or with SOC included [22]. Here, we focus on the low-energy electric carriers at energies near the Dirac points. A four-band model including spin-orbit interaction is investigated. Analytical expressions, not only including SOC but also different band occupations, vertical electric fields modifying the effective SOC constants, and temperature variations, are derived for the heat conductance, the Lorenz number, and the heat capacity. For comparison, also the electrical conductance is studied.

II. METHODOLOGY

A. Electronic structure model

For energies near the chemical potential μ of the electrons, i.e., near the Dirac points located at the K ($\xi = +$) and K' ($\xi = -$) corner points of the 2D hexagonal BZ, the band structure of Xenes can be described by a four-band tight-binding model including SOC. With the 2D wave-vector deviations $\tilde{\mathbf{k}} = \mathbf{k} - \mathbf{k}_{K_\xi}$ from the corner points with valley index ξ , one has a 4×4 Hamiltonian matrix [1,15,35,36]

$$\hat{H}_\xi(\tilde{\mathbf{k}}) = \xi \begin{pmatrix} \hat{h}(\tilde{\mathbf{k}}) & \hbar v_F \tilde{k}_{+\xi} \hat{\sigma}_0 \\ \hbar v_F \tilde{k}_{-\xi} \hat{\sigma}_0 & -\hat{h}(\tilde{\mathbf{k}}) \end{pmatrix} \quad (1)$$

with $\tilde{\mathbf{k}} = (\tilde{k}_x, \tilde{k}_y)$, $\tilde{k}_{\pm\xi} = \xi \tilde{k}_x \pm i \tilde{k}_y$, and the 2×2 matrix $\hat{h}(\tilde{\mathbf{k}}) = -\lambda_{\text{SO}} \hat{\sigma}_z + \xi U \hat{\sigma}_0$, where $\hat{\sigma}_z$ denotes a Pauli matrix but $\hat{\sigma}_0$ the unit matrix. The Rashba contribution to the SOC has been neglected because of its general smallness for Xenes [35]. The Fermi velocity v_F characterizes the gapless linear bands in the limit of vanishing SOC, $\lambda_{\text{SO}} \equiv 0$. The bias voltage $U = eF_z \Delta / 2$ can be related to a vertical electric field with strength F_z , where Δ describes the buckling of the Xene lattice. For the parameters in (1), we apply the results of atomic and electronic structure calculations within the density functional theory and a semilocal exchange-correlation potential [1,7]. They are $\Delta = 0.00$ (0.45, 0.69, 0.85, 0.92) Å, $v_F = 0.83$ (0.53, 0.52, 0.48, 0.45) $\times 10^6$ m s $^{-1}$, and the spin-orbit gap $2\lambda_{\text{SO}} = 0.0$ (1.5, 24.0, 73.0, 491) meV for graphene (silicene, germanene, stanene, plumbene). The area of the unit cell is 5.28 (12.96, 14.28, 18.91, 21.28) Å 2 .

The diagonalization of the Hamiltonians (1) gives the four bands as eigenvalues

$$\begin{aligned} \varepsilon_{\xi v s}(\tilde{\mathbf{k}}) &= v \sqrt{\lambda_{\xi s}^2 + \hbar^2 v_F^2 \tilde{k}^2}, \\ \lambda_{\xi s} &= U - \xi s \lambda_{\text{SO}}, \end{aligned} \quad (2)$$

where $v = +, -$ indicates the conduction ($v = +$) or valence ($v = -$) band and $s = +, -$ the spin orientation. The applied electric field modifies the energy gap $E_g = 2|\lambda_{\xi s}|$ via the effective SOC constant $\lambda_{\xi s}$. The zero of the latter one, $\lambda_{\xi s} = 0$, characterizes the transition from the topological to the trivial phase of a Xene [37]. Small gaps, $|\lambda_{\xi s}| \rightarrow 0$, give rise to linear bands in $|\tilde{\mathbf{k}}|$ and, hence, massless Dirac fermions, while finite effective SOC constants $\lambda_{\xi s}$ define massive Dirac particles for small wave-vector deviations $\tilde{\mathbf{k}}$ from the K or K' point

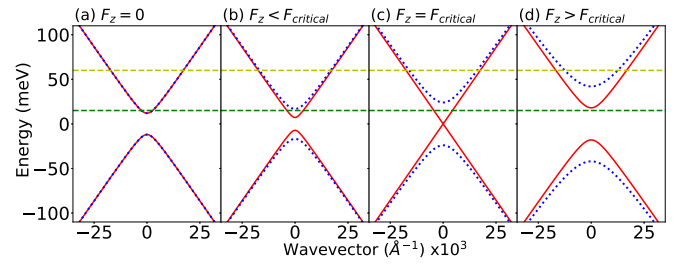


FIG. 1. Electronic band structure of germanene in proximity of the Dirac point as a function of an external electric field. SOC is included. The horizontal lines denote two different values of the chemical potential ($\mu = 15$ meV, green line, and $\mu = 60$ meV, yellow line). Red and blue bands refer to spin up and down states, respectively.

[7]. An example of topological to trivial insulator transition, induced by an applied electric field, is shown in Fig. 1 for germanene. The two chosen chemical potentials illustrate the degenerate or nondegenerate character of the spin polarized electron gases with variation of the external electric field.

The eigenvalues (2) allow the description of the spectral properties of the Xenes in the low-energy region [1,38]. Single-particle properties may be described by the trace of the matrix of single-particle spectral functions

$$\text{Tr}\{\hat{A}_\xi(\tilde{\mathbf{k}}, \varepsilon)\} = 2\pi \sum_{v=+,-} \sum_{s=+,-} \delta(\varepsilon - \varepsilon_{\xi v s}(\tilde{\mathbf{k}})), \quad (3)$$

which yields the density of states (DOS) per energy as

$$D(\varepsilon) = \frac{1}{2\pi} \sum_{\xi=+,-} \frac{A}{(2\pi)^2} \int d^2\tilde{\mathbf{k}} \text{Tr}\{\hat{A}_\xi(\tilde{\mathbf{k}}, \varepsilon)\}.$$

The DOS has contributions from both valleys and both spin spaces [1,38]

$$\begin{aligned} D(\varepsilon) &= \sum_{\xi=+,-} \sum_{s=+,-} D_{\xi s}(\varepsilon), \\ D_{\xi s}(\varepsilon) &= \frac{A}{2\pi \hbar^2 v_F^2} |\varepsilon| \Theta(|\varepsilon| - |\lambda_{\xi s}|). \end{aligned} \quad (4)$$

Without A , the area of the 2D unit cell of a Xene, the DOS is measured per energy interval and unit area.

B. Heat capacity

The electronic contribution to the specific heat or heat capacity at constant area A of the 2D electron gas [32,39] is given as

$$C_A(T) = \left(\frac{\partial u}{\partial T} \right)_A \quad (5)$$

with the internal energy

$$u(T) = \int_{-\infty}^{+\infty} \varepsilon D(\varepsilon) f(\varepsilon) d\varepsilon, \quad (6)$$

which is defined by the temperature-dependent Fermi-Dirac function $f(\varepsilon) = 1/[\exp((\varepsilon - \mu)/k_B T) + 1]$, where the chemical potential is measured with respect to the Dirac point in a

midgap position of the bands (2). Using the DOS in (4), one finds

$$C_A(T) = k_B \frac{2}{\pi} \frac{(k_B T)^2 A}{\hbar^2 v_F^2} \frac{1}{4} \sum_{\xi=+,-} \sum_{s=+,-} \tilde{C} \left(\frac{|\lambda_{\xi s}|}{k_B T}, \frac{|\mu|}{k_B T} \right), \quad (7)$$

$$\tilde{C}(x, y) = \int_x^\infty t^2 \left\{ (t-y) \frac{e^{t-y}}{[e^{t-y}+1]^2} + (t+y) \frac{e^{t+y}}{[e^{t+y}+1]^2} \right\} dt. \quad (8)$$

An analytic expression of (8) is possible

$$\tilde{C}(x, y) = x^2 \left\{ \frac{x-y}{e^{x-y}+1} + \frac{x+y}{e^{x+y}+1} \right\} + 6\{F_2(y, x) + F_2(-y, x)\} - 2y\{F_1(y, x) - F_1(-y, x)\}, \quad (9)$$

if incomplete Fermi-Dirac integrals

$$F_n(a, b) = \frac{1}{n!} \int_b^\infty dt \frac{t^n}{e^{t-a}+1} \quad (n = 0, 1, 2, \dots) \quad (10)$$

are introduced.

C. Thermal and electrical transport coefficients

Applying Onsager relations between electrical and heat currents and in-plane electric fields and temperature gradients, respectively [32,40], one derives

$$\sigma = e^2 L_{11}, \quad (11)$$

$$\kappa = \frac{1}{T} \left\{ L_{22} - \frac{L_{12}^2}{L_{11}} \right\} \quad (12)$$

for the static electrical conductance σ and the heat conductance κ , where the Onsager coefficients are given ($i, j = 1, 2$) by the Jonson-Mahan theorem [41–44]

$$L_{ij} = -\frac{\hbar}{4\pi} \sum_{\xi=+,-} \int \frac{d^2 \tilde{\mathbf{k}}}{(2\pi)^2} \int_{-\infty}^{+\infty} \left[\frac{\partial}{\partial \varepsilon} f(\varepsilon) \right] \times (\varepsilon - \mu)^{i+j-2} K_{\xi}(\tilde{\mathbf{k}}; \varepsilon, \varepsilon) d\varepsilon. \quad (13)$$

The transport properties are ruled by the spectral behavior of the current-current correlation function averaged over the two in-plane Cartesian coordinates x and y as

$$K_{\xi}(\tilde{\mathbf{k}}; \varepsilon, \varepsilon') = \frac{1}{2} \text{Tr} \{ [\hat{V}_x(\xi, \tilde{\mathbf{k}}) \hat{A}_{\xi}(\tilde{\mathbf{k}}, \varepsilon')] [\hat{V}_x(\xi, \tilde{\mathbf{k}}) \hat{A}_{\xi}(\tilde{\mathbf{k}}, \varepsilon)] + [\hat{V}_y(\xi, \tilde{\mathbf{k}}) \hat{A}_{\xi}(\tilde{\mathbf{k}}, \varepsilon')] [\hat{V}_y(\xi, \tilde{\mathbf{k}}) \hat{A}_{\xi}(\tilde{\mathbf{k}}, \varepsilon)] \} \quad (14)$$

with the matrices $\hat{V}_x(\xi, \tilde{\mathbf{k}})$ and $\hat{V}_y(\xi, \tilde{\mathbf{k}})$ of the Cartesian components of the velocity operator. One finds [1]

$$K_{\xi}(\tilde{\mathbf{k}}; \varepsilon, \varepsilon') = 2\pi^2 v_F^2 \sum_{v, v'=+,-} \sum_{s=+,-} \frac{\varepsilon \varepsilon' - \lambda_{\xi s}^2}{\varepsilon_{\xi v s}(\tilde{\mathbf{k}}) \varepsilon_{\xi v' s}(\tilde{\mathbf{k}})} \times \delta(\varepsilon - \varepsilon_{\xi v s}(\tilde{\mathbf{k}})) \delta(\varepsilon' - \varepsilon_{\xi v' s}(\tilde{\mathbf{k}})). \quad (15)$$

In order to compute the static limit and, therefore, intraband contributions of the electrical and heat conductances with $v = v'$ and $\varepsilon = \varepsilon'$ a Dirac δ function $\delta(0)$ at zero argument appears. Applying the definition of the Dirac δ function, one writes explicitly $\delta(0) \rightarrow \frac{1}{\pi\gamma}$ with $\gamma = \hbar/\tau$ as the reciprocal relaxation time τ of the carriers multiplied with \hbar , i.e., in

energy units. Sometimes, this replacement is called constant relaxation time approximation, with the intraband relaxation time τ [32,45].

The constant-relaxation-time approach is a rough approximation to describe globally the carrier scattering processes by electron-electron, electron-phonon, electron-impurity etc. interaction which, however, depend on the material, the doping level and the temperature. More in general, the relaxation time varies with the band energy and the quasimomentum. These dependencies have been analytically investigated for different scattering mechanisms for graphene [46,47]. In 3D metals, τ is typically 10^{-14} to 10^{-15} s at room temperature, i.e., $\gamma = 66\text{--}660$ meV [32]. In intrinsic 2D crystals, e.g., graphene, the relaxation time and, consequently, the electrical conductivity is strongly limited by the electron-phonon scattering [48,49]. The phonon mechanism gives, for high doping and room temperature, $\tau = 2$ ps [50] or for silicene $\tau = 1\text{--}13$ ps, values which may be reduced due to substrate effects toward less than 1 ps [51,52]. In the case of impurity scattering in graphene also values of the order of 1–17 ps have been published [53]. Consequently, an upper limit of about $\gamma = 100$ meV may be investigated.

In the case of the electrical conductance σ the relation (11) to L_{11} combined with (13) arises from the Kubo formula [1,45,54]. The relation of the thermal conductance κ (12) to L_{11} , L_{12} , and L_{22} comes from its evaluation to first temperature corrections as shown in the framework of the Sommerfeld expansion [32,43]. The generalization of L_{11} to the other Onsager coefficients L_{12} and L_{22} (13) can be demonstrated in terms of thermodynamic Green functions to result in energy-dependent prefactors $(\varepsilon - \mu)^{i+j-2}$ of the integrand [42,55]. Apart from an equal temperature-dependent factor, expression (13) is in agreement with similar representations in Refs. [33,40].

With the explicit correlation function (15) the Onsager coefficients become

$$L_{ij} = \frac{1}{\pi \gamma \hbar} [-\text{sgn}(\mu)]^{i+j-2} (k_B T)^{i+j-1} \times \frac{1}{4} \sum_{\xi=+,-} \sum_{s=+,-} C_{i+j-2} \left(\frac{|\lambda_{\xi s}|}{k_B T}, \frac{|\mu|}{k_B T} \right) \quad (16)$$

with ($n = 0, 1, 2$)

$$C_n(x, y) = \int_x^\infty dt \left(t - \frac{x^2}{t} \right) \left\{ (t-y)^n \frac{e^{t-y}}{[e^{t-y}+1]^2} + (-1)^n (t+y)^n \frac{e^{t+y}}{[e^{t+y}+1]^2} \right\}. \quad (17)$$

Similarly to $\tilde{C}(x, y)$ (8), this expression can be also represented in terms of incomplete Fermi-Dirac integrals (10). Apart from constant prefactors and the sums over the valleys K and K' and spin spaces $s = +, -$, similar expressions can be found in Refs. [22,33,34]. There, however, SOC (apart from [22]) and field effects are not taken into account, i.e., $\lambda_{\xi s} \equiv 0$. Moreover, instead of γ the energy $\frac{\pi}{2} \hbar v_F d$ with the thickness d of the Xenes appears [22].

D. Lorenz number

Very interesting is the ratio $LT = \kappa/\sigma$ of thermal and electrical conductance, with L known as Lorenz number. In the classical Drude limit of a three-dimensional (3D) electron gas, L is proportional to the temperature T , in complete agreement with the law of Wiedemann and Franz, with a prefactor $L = \frac{3}{2}(\frac{k_B}{e})^2$ [32,39,45]. With first nonclassical corrections within the Drude-Sommerfeld approximation the prefactor becomes, instead, $L = \frac{\pi^2}{3}(\frac{k_B}{e})^2$ [32]. However, in general, for other electron gases, the proportionality factor L is not a fundamental constant. Applying the definitions (11) and (12), with the Onsager coefficients (16) derived in the framework of the electronic structure model (1), the Lorenz number becomes

$$L = \frac{\kappa}{\sigma T} = \frac{1}{e^2 T^2} \frac{L_{22}L_{11} - L_{12}^2}{L_{11}^2}, \quad (18)$$

and therefore

$$L = \left(\frac{k_B}{e}\right)^2 \frac{\frac{1}{4} \sum_{\xi=+,-} \sum_{s=+,-} C_2(x, y)}{\frac{1}{4} \sum_{\xi=+,-} \sum_{s=+,-} C_0(x, y)} - \left(\frac{k_B}{e}\right)^2 \frac{\left[\frac{1}{4} \sum_{\xi=+,-} \sum_{s=+,-} C_1(x, y) \right]^2}{\left[\frac{1}{4} \sum_{\xi=+,-} \sum_{s=+,-} C_0(x, y) \right]^2} \quad (19)$$

with $x = |\lambda_{\xi s}|/k_B T$ and $y = |\mu|/k_B T$.

E. Transport limits: vanishing SOC or band occupation

In the case of graphene, i.e., no SOC and no layer buckling, it holds $\lambda_{\text{SO}} = 0$ and $\Delta = 0$. Consequently, the quantities (7), (11), and (12) have to be only investigated in the limit $\lambda_{\xi s} = 0$, which is also fulfilled for the other Xenos in the high-temperature limit $|\lambda_{\xi s}| \ll k_B T$. Expressions (8) and (17) have to be investigated for $x = 0$. The important factors (17) are ($n = 0, 1, 2$)

$$C_n(0, y) = \int_{-\infty}^{+\infty} dt |t + y| t^n \frac{e^t}{(e^t + 1)^2} \quad (20)$$

in agreement with Ref. [22]. They can be related to the complete Fermi-Dirac integrals $F_n(a, 0)$ (10). We go a step further and use their relation to the polylogarithms $Li_{n+1}(z)$ [56] with

$$Li_{n+1}(-e^y) = -F_n(y, 0) \quad (21)$$

and their series expansion

$$Li_n(z) = \sum_{k=1}^{\infty} \frac{z^k}{k^n} \quad (|z| < 1). \quad (22)$$

The arguments e^y of the polylogarithms hamper the investigation of the low-temperature limit $y \rightarrow \infty$. For that reason, we apply the inversion relations [56,57]

$$\begin{aligned} Li_1(-e^y) &= 2yLi_0(-1) + Li_1(-e^{-y}), \\ Li_2(-e^y) &= y^2Li_0(-1) + 2Li_2(-1) - Li_2(-e^{-y}), \\ Li_3(-e^y) &= \frac{1}{3}y^3Li_0(-1) + 2yLi_2(-1) + Li_3(-e^{-y}) \end{aligned} \quad (23)$$

with the values $Li_0(-1) = -\frac{1}{2}$ and $Li_2(-1) = -\frac{\pi^2}{12}$ [57,58]. For small n , such relations are obvious because of the validity of $Li_0(z) = z/(1-z)$ and $Li_1(z) = -\ln(1-z)$. The factors (20) ruling the Onsager coefficients (16) are

$$\begin{aligned} C_0(0, y) &= y - 2Li_1(-e^{-y}) = y + 2\ln(1 + e^{-y}), \\ C_1(0, y) &= \frac{\pi^2}{3} + 2yLi_1(-e^{-y}) + 4Li_2(-e^{-y}), \\ C_2(0, y) &= \frac{\pi^2}{3}y - 2y^2Li_1(-e^{-y}) - 8yLi_2(-e^{-y}) \\ &\quad - 12Li_3(-e^{-y}) \end{aligned} \quad (24)$$

in agreement with the results in Ref. [22].

Very interesting are the classical high-temperature and the quantum low-temperature limits. In the high-temperature limit $|\mu| \ll k_B T$ ($y \rightarrow 0$), one finds

$$\begin{aligned} C_0(0, 0) &= -2Li_1(-1) = 2\ln 2, \\ C_1(0, 0) &= 0, \\ C_2(0, 0) &= -12Li_3(-1) = 12\eta(3), \end{aligned} \quad (25)$$

where $\eta(3) = \frac{3}{4}\xi(3) = 0.90154$ is directly related to the Riemann zeta function $\xi(z)$ [59]. For graphene-like materials and high temperatures the three most important transport and thermal properties (11), (12), and (18) become

$$\begin{aligned} \sigma &= 4\ln 2 \frac{e^2 k_B T}{h \gamma}, \\ \kappa &= \frac{k_B}{\pi \gamma \hbar} (k_B T)^2 12\eta(3), \\ L &= \left(\frac{k_B}{e}\right)^2 6 \frac{Li_3(-1)}{Li_1(-1)} = \left(\frac{k_B}{e}\right)^2 \frac{6\eta(3)}{\ln 2} = 7.804 \left(\frac{k_B}{e}\right)^2 \\ &= 5.79 \times 10^{-8} \text{ W } \Omega \text{ K}^{-2} \end{aligned} \quad (26)$$

with the conductance quantum $e^2/h = (1/25813) \Omega^{-1}$, the Boltzmann constant $k_B = 1.38 \times 10^{-23} \text{ J K}^{-1}$, and the quantity $(k_B/e)^2 = 0.742 \times 10^{-8} \text{ W } \Omega \text{ K}^{-2}$. Consequently, the Lorenz number of the graphenelike electron gas is more than twice that of a 3D electron gas in Drude or Drude-Sommerfeld approach. Applying a typical broadening value $\gamma = 100 \text{ meV}$, one observes at room temperature 2D in-plane values of $\sigma = 2.88 \times 10^{-5} \Omega^{-1}$ and $\kappa = 4.79 \times 10^{-10} \text{ W K}^{-1}$. For comparison with 3D literature values, one may divide the 2D quantities by the effective thickness $d = 3.35 \text{ \AA}$ of a graphene layer [60], resulting in $\sigma/d = 0.86 \times 10^5 (\Omega \text{ m})^{-1}$ and $\kappa/d = 1.43 \text{ W m}^{-1} \text{ K}^{-1}$. The ‘‘3D’’ electrical conductivity of graphene is much too large by five orders of magnitude in comparison to experiment [61], including the lattice contribution, while the ‘‘3D’’ thermal conductivity is by about three orders of magnitude smaller than measured values [62], in agreement with the expectation that the phonon contribution is predominant. However, for much larger scattering times, e.g., $\gamma \rightarrow 1 \text{ meV}$, the situation changes drastically. The thermal electronic part comes in the range of the vibronic contribution.

In the low-temperature limit $|\mu| \gg k_B T$, i.e., $y \rightarrow \infty$, it holds $Li_n(-e^{-y}) = -e^{-y}$ and, therefore,

$$C_0(0, y) = y, \quad C_1(0, y) = \frac{\pi^2}{3}, \quad C_2(0, y) = \frac{\pi^2}{3}y,$$

$$\frac{C_2(0, y)C_0(0, y) - C_1^2(0, y)}{C_0^2(0, y)} = \frac{\pi^2}{3}. \quad (27)$$

The interesting quantities for an electron or hole gas in graphenelike materials in the quantum limit are

$$\sigma = 2 \frac{e^2}{h} \frac{|\mu|}{\gamma},$$

$$\kappa = \frac{k_B}{\pi \gamma \hbar} (k_B T) |\mu| \frac{\pi^2}{3},$$

$$L = \frac{\pi^2}{3} \left(\frac{k_B}{e} \right)^2. \quad (28)$$

The conventional Wiedemann-Franz law, as derived within the Drude-Sommerfeld theory, is recovered analytically, i.e., the low-temperature Lorenz number L of graphene is very close to the room-temperature value of many metals [32]. The electrical conductance approaches a temperature-independent value, which however is ruled by the band occupation according to $|\mu|/\gamma$. The heat conductance vanishes linearly with the temperature but also with the chemical potential measured with respect to the Dirac point.

F. Limits of electronic heat capacity

In the graphene limit without SOC and external electric field, $x = 0$, the heat capacity (7) is dominated by the specialization using (21) and (23)

$$\tilde{C}(0, y) = 2 \frac{\pi^2}{3} y - 4y Li_2(-e^{-y}) - 12 Li_3(-e^{-y}) \quad (29)$$

with

$$\lim_{y \rightarrow 0} \tilde{C}(0, y) = -12 Li_3(-1) = 12\eta(3) = 10.818$$

and

$$\lim_{y \rightarrow \infty} \tilde{C}(0, y) = \lim_{y \rightarrow \infty} \frac{2\pi^2}{3} y \rightarrow \infty.$$

For graphene, in the high-temperature limit, the heat capacity (7) increases quadratically in temperature, as $C_A(T) = 0.81 \times 10^{-3} k_B (\frac{T}{T_0})^2$. This behavior is different from a conventional electron gas with a square-root-like DOS resulting in a linear temperature variation [32,39,45], because of the linear energy variation of the DOS (4) in 2D-Dirac systems. In the low-temperature limit, the graphene heat capacity vanishes linearly.

In the limit of undoped Xenes silicene, germanene, stanene, and plumbene, $y = 0$, the heat capacity is ruled by

$$\tilde{C}(x, 0) = \frac{2x^3}{e^x + 1} - 6x^2 Li_1(-e^{-x}) - 12x Li_2(-e^{-x}) - 12 Li_3(-e^{-x}) \quad (30)$$

with

$$\lim_{x \rightarrow 0} \tilde{C}(x, 0) = -12 Li_3(-1) = 12\eta(3) = 10.82$$

and

$$\lim_{x \rightarrow \infty} \tilde{C}(x, 0) = \lim_{x \rightarrow \infty} 6x^2 e^{-x} = 0.$$

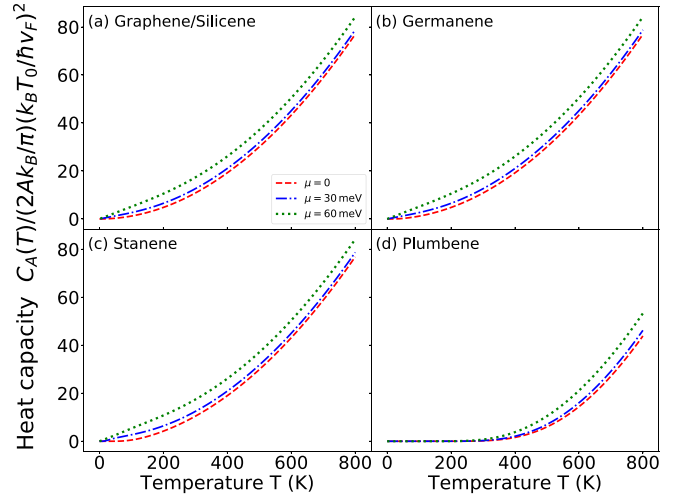


FIG. 2. Electronic heat capacity $C_A(T)$ at constant area A vs temperature T for (a) graphene/silicene, (b) germanene, (c) stanene, and (d) plumbene in units of $k_B \frac{2}{\pi} \left(\frac{k_B T_0 \sqrt{A}}{h v_F} \right)^2 = 0.75-10.30 \times 10^{-4} k_B$ (graphene, ..., plumbene) with $T_0 = 300$ K. The occupation of the bands is varied with $|\mu| = 0, 30$, and 60 meV (red-dashed, blue-dot-dashed, and green-dotted lines, respectively).

Consequently, the heat capacity vanishes exponentially with temperature lowering, but increases quadratically with rising temperature in agreement with the thermally induced free carrier distribution.

III. RESULTS AND DISCUSSIONS

A. Heat capacity

By using Eqs. (7) and (8), the electronic contribution to the heat capacity $C_A(T)$ is calculated. The results are presented in Figs. 2 and 3. Here and in the following, the results for silicene are not separately reported as they are superimposed to the ones for graphene. Therefore the reference to silicene is added in figures showing the results for graphene.

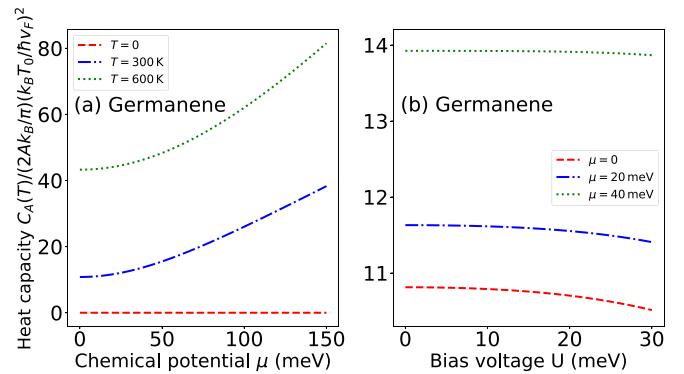


FIG. 3. Electronic heat capacity $C_A(T)$ (in units of $k_B \frac{2}{\pi} \left(\frac{k_B T_0 \sqrt{A}}{h v_F} \right)^2$) of germanene vs (a) chemical potential $|\mu|$ and (b) bias voltage $|U|$. The three curves in (a) correspond to the temperatures $T = 0$ (red-dashed), 300 (blue-dot-dashed), and 600 K (green-dotted). In (b), three different occupations $|\mu| = 0$ (red-dashed), $|\mu| = 20$ (blue-dot-dashed), and $|\mu| = 40$ meV (green-dotted) are studied at room temperature.

Figure 2 illustrates the temperature dependence of the heat capacity for all Xenes but different doping situations expressed by the chemical potential μ . A general temperature dependence is visible. According to the discussion of formulas (7) and (29), for finite μ , $C_A(T)$ vanishes linearly with small T but increases quadratically with rising T . In contrast to predictions in the literature for graphene [58] and silicene [33], the appearance of a peak, due to the Schottky anomaly [39] in a two-level model, does not occur. Rather, in agreement with the limiting cases of (7) with (29) one observes in Fig. 2 a nearly linear variation of the normalized $C_A(T) \sim \frac{2\pi^2}{3} \frac{|\mu|}{k_B T_0} \frac{T}{T_0}$ for low temperatures $T \rightarrow 0$ K but a quadratic increase $\sim 10.818(T/T_0)^2$ for high temperatures [(7) with (30)]. These findings are in agreement with a similar study on germanene [34]. In any case, the level occupation $|\mu|$ and, therefore, the carrier concentration $n \sim |\mu|^2$ only play a minor role, independent of the actual temperature. In addition, the normalization factor makes the dependence of the heat capacity on the specific Xene almost negligible, with the exception of plumbene, where the sizable gap affects the heat capacity behavior for T below 400 K, if no doping is present. The dependence of the normalized $C_A(T)$ curves on the Xene in Fig. 2 is also illustrated by expression (8). The SOC shifts the lower boundary of the integral in (8) toward larger values and, therefore, reduces the value of the integral. Consequently, the normalized curves are reduced going from graphene to plumbene. Thereby, for the low-gap materials, the effects of the occupation of the bands are of minor influence on the heat capacity. According to the prefactor $\frac{2}{\pi} (\frac{k_B T_0 \sqrt{A}}{\hbar v_F})^2 k_B$ of $0.75\text{--}10.30 \times 10^{-4} k_B$ at $T_0 = 300$ K in (7), the electronic contribution $C_A(T) \equiv C_A^{\text{el}}(T)$ to the heat capacity of Xenes is much smaller than the vibrational contribution $C_A^{\text{vib}}(T) \sim k_B$. Their ratio is roughly determined by $C_A^{\text{vib}}(T)/C_A^{\text{el}}(T) \approx (v_F/v)^2$ [63,64], where v is the phonon group velocity. The group velocities of the longitudinal-acoustic phonon branch in heavier Xenes, germanene and stanene, are 0.7 or 0.5×10^3 m s $^{-1}$, while the Fermi velocity v_F is around 0.5×10^6 m s $^{-1}$ [65,66]. According to the simple ratio square of the velocities, the phonon contribution to the specific heat can approximately be six orders of magnitude larger than the electronic contribution [64], hence even larger than in a 3D metal, where anyway the phonon contribution dominates for not too low temperatures.

Because of the smallness of the electronic contribution to $C_A(T)$, its dependence on the band occupation and the external electric field is described in Fig. 3 only for germanene as example. The relatively weak influence of the occupation with $C_A(T) \sim |\mu|$ for low temperatures is described in Fig. 3(a) for germanene. There is also a rapid increase with temperature as already seen in Fig. 2. With increasing number of carriers $n \sim |\mu|^2$ (in the low- T -limit) the heat capacity also increases. The field dependence in Fig. 3(b) is dominated by $||U| \pm \lambda_{\text{SO}}|/k_B T$, the lower integral boundary in (8). As a consequence of the decrease (increase) of the contribution with the $+(-)$ sign, in total a tendency for partial compensation of the field effects exist. A variation of the total electronic contribution is rather weak with the electric field. Moreover, the transition of the field-modified germanene from the topological QSH phase into the trivial phase above the critical

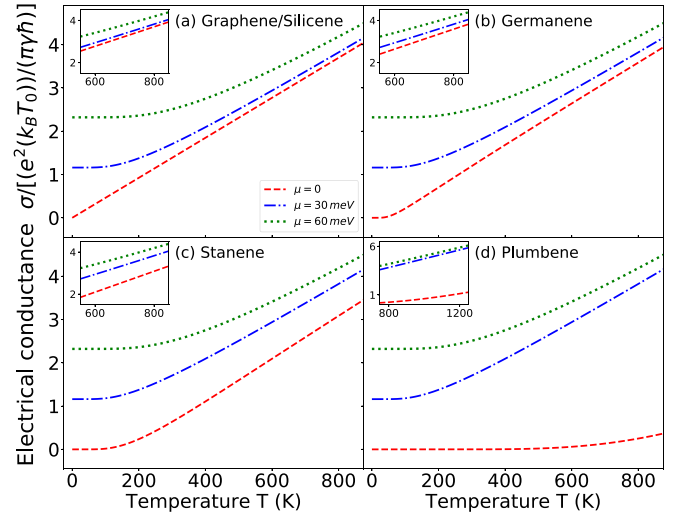


FIG. 4. Electrical conductance σ vs temperature T for (a) graphene/silicene, (b) germanene, (c) stanene, and (d) plumbene in units of $2 \frac{e^2}{h} \frac{k_B T_0}{\gamma}$. The band occupation is varied with $|\mu| = 0$ (red-dashed), 30 (blue-dot-dashed), and 60 meV (green-dotted). The insets show the high-temperature convergence towards the same red independently of the occupation.

field strength $U = \lambda_{\text{SO}}$ [37,67] has no influence on the heat capacity.

B. Electrical conductance

The in-plane electrical conductance σ is plotted versus temperature in Fig. 4 for graphene/silicene, germanene, stanene, and plumbene in units of $2 \frac{e^2}{h} \frac{k_B T_0}{\gamma} = 2.002 \times 10^{-5} \Omega^{-1}$ for $\gamma = 100$ meV and $T_0 = 300$ K. In the case of $\lambda_{\text{SO}} = 0$, i.e., graphene in Fig. 4(a), it holds from (24) $\sigma = 2 \frac{e^2}{h} \frac{|\mu|}{\gamma} \{1 + \frac{2k_B T}{|\mu|} \ln[1 + \exp(-|\mu|/k_B T)]\}$. Consequently, this conductance linearly vanishes in the low-temperature limit for $\mu = 0$. For doped graphene, the low-temperature value of σ is ruled by the chemical potential $|\mu|$ for $T = 0$ K and, for increasing T , we find a subsequent linear behavior $\sigma \sim 2k_B T \ln 2$. A similar temperature behavior as for graphene is observed for silicene, germanene, stanene, and plumbene despite the finite λ_{SO} , when $\mu \neq 0$. In the case of these Xenes, the low-temperature limit is ruled by a constant value whose magnitude depends on the doping level, while the extension of the constant region above $T = 0$ K is ruled by the gap value $\sim \lambda_{\text{SO}}$. The high-temperature trend is independent of the Xene and its doping. The electrical conductance shows the same linear behavior $\sim 2k_B T \ln 2$. Previous tight-binding studies found an opposite high-temperature behavior of σ for increasing T in silicene [33], while more recent studies of germanene [34] agree with the results of Fig. 4(a).

The absolute values of the 2D conductance of graphene are difficult to compare with experimental results. This is perhaps easier for a derived quantity, the carrier mobility $\mu_m = \sigma/en$ with n as the density of holes or electrons. In the low-temperature limit the carrier density is given by $n = |\mu|^2/(\pi \hbar^2 v_F^2)$ and the conductance by the Drude-like expression (28) $\sigma = e^2 |\mu|/(\pi \hbar \gamma)$, resulting in a mobility

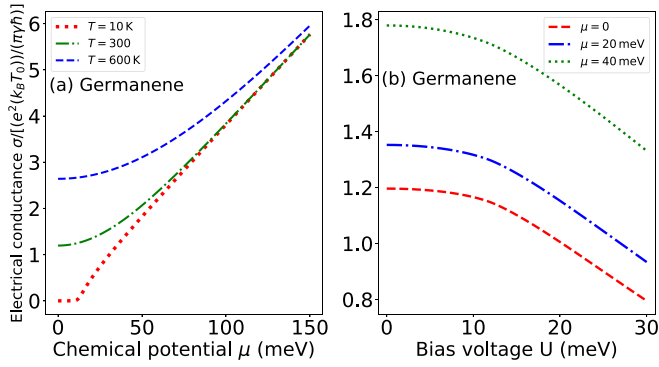


FIG. 5. Electrical conductance σ of germanene vs (a) chemical potential $|\mu|$ and (b) bias voltage $|U|$. In (a) the three curves correspond to the temperatures $T = 10$ (red-dashed), 300 (blue-dot-dashed), and 600 K (green-dotted) and $U = 0$. In (b), three different occupations $|\mu| = 0$ (red-dashed), 20 (blue-dot-dashed), and 40 meV (green-dotted) are studied at room temperature $T = 300$ K.

$\mu_m = e\hbar v_F^2 / (\gamma|\mu|)$ for $T \rightarrow 0$ K. With the Fermi velocity of graphene it holds $\mu_m = (\frac{100 \text{ meV}}{\gamma})(\frac{100 \text{ meV}}{|\mu|})453.3 \text{ cm}^2 \text{ V}^{-1} \text{ s}^{-1}$. That means in the limit of low doping n , i.e., small $|\mu|$ and/or small broadening parameter γ (large scattering times), the mobility derived within the electronic structure model (1) is able to explain the measured values between 3000 and 10 000 $\text{cm}^2 \text{ V}^{-1} \text{ s}^{-1}$ for $n = 5 \times 10^{12} \text{ cm}^{-2}$, i.e., $|\mu| = 216 \text{ meV}$, and $\gamma = 14.3\text{--}4.3 \text{ meV}$ [61], or even 200 000 $\text{cm}^2 \text{ V}^{-1} \text{ s}^{-1}$ for $n = 2 \times 10^{11} \text{ cm}^{-2}$, i.e., $|\mu| = 8.7 \text{ meV}$, and $\gamma = 2.6 \text{ meV}$ [68].

In Fig. 5(a), the influence of the doping level is more clearly illustrated in the case of germanene. The electrical conductance increases with the number of carriers independent of temperature. The temperature determines the absolute values of σ especially in the limit of small carrier densities, $\mu \rightarrow 0$. Consequently, for low doping, i.e., for a classical 2D electron gas, the conductance is rather temperature-dependent. For higher chemical potentials, for degenerate electron gases with $|\mu| > \lambda_{\text{SO}}$, a strong conductance increase occurs, which is nearly linear in μ following (28). The influence of an external electric field on the conductance in Fig. 5(b) can be again discussed in terms of the variation of the effective spin-orbit interaction $\lambda_{\xi s}$ (2). It is ruled by the integral $C_0(x, y)$ in (17). With rising parameter $x = |\lambda_{\xi s}|/k_B T$, the integral value is reduced by the shift of the lower integral limit toward larger values and the reduction of the integrand by the term proportional to x^2 . The effect of finite x values also depends on the doping level, i.e., on the y value, $y = |\mu|/(k_B T_0)$. It rules the absolute value of σ . Thereby, for $U < \lambda_{\text{SO}}$, the curves σ versus U show a plateau, while for larger bias voltages $U > \lambda_{\text{SO}}$ a decrease appears. The bias opens and closes the gap and affects the band distances by varying $\lambda_{\xi s}$.

C. Thermal conductance

The temperature dependence of the thermal conductance of the five Xenex graphene, silicene, germanene, stanene and plumbene is illustrated in Fig. 6.

In agreement with the analytical limits (26) and (28), one observes an almost linear increase with temperature in the low-temperature limit. Independent of μ , the thermal con-

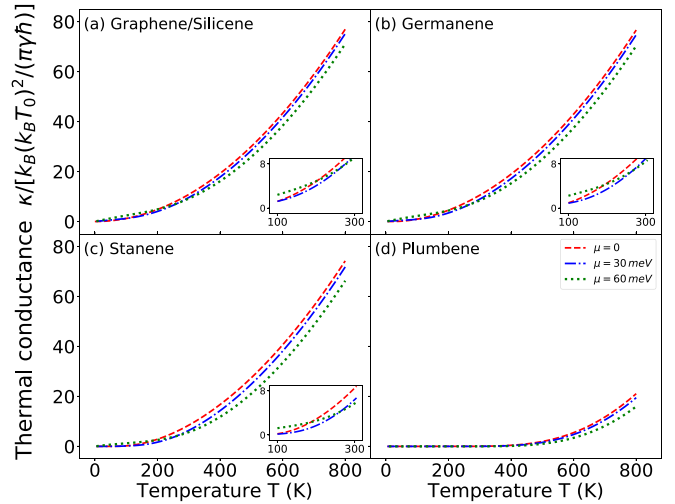


FIG. 6. Thermal conductance κ of (a) graphene/silicene, (b) germanene, (c) stanene, and (d) plumbene vs temperature T in units of $k_B(k_B T_0)^2 / (\pi\gamma\hbar) = \frac{100 \text{ meV}}{\gamma} \times 4.46 \times 10^{-11} \text{ W K}^{-1}$ with $T_0 = 300$ K. Curves for three occupation levels $|\mu| = 0$ (red-dashed), 30 (blue-dot-dashed), and 60 meV (green-dotted) are presented. The insets show the crossing of the curves for different occupations at low temperatures.

ductance κ vanishes with $T \rightarrow 0$ [see Eq. (28)]. However, for higher temperatures $k_B T \gg |\mu|$, this increase becomes quadratic. The quadratic behavior is nearly found in the entire temperature range for $\mu = 0$. In general, the lower-temperature slopes of κ slightly increase with the occupation level $|\mu|$, while in the high-temperature limit κ is slightly reduced with respect to the $\mu = 0$ case. As a consequence (see insets in Fig. 6) the κ -curves for zero chemical potential and finite μ values cross each other for temperatures between 100–250 K, somewhat in dependence of the Xene material.

The absolute values decrease slightly along the column $C \rightarrow \text{Si} \rightarrow \text{Ge} \rightarrow \text{Sn} \rightarrow \text{Pb}$. The effect becomes much more pronounced for a larger spin-orbit coupling constant of $\lambda_{\text{SO}} = 250 \text{ meV}$, close to that of plumbene [16,69]. Then, κ is drastically reduced in the displayed temperature range as a consequence of the significant SOC-induced gap, which is large compared to the chosen $k_B T$ and μ values. Even if $\mu = 0$, for finite temperatures small amounts of carriers are still available to conduct heat. The extremely small reduction with rising value λ_{SO} in the case of the four Xenex graphene, silicene, germanene, and stanene in Figs. 6(a)–6(c) is due to similar effects as discussed above for the heat capacity, whereas a more significant reduction of κ occurs for plumbene. This is mainly due to the low carrier densities in plumbene for the same μ . They are only temperature-induced. The general temperature dependence is in agreement with other calculations for germanene and stanene [22,34] but contradicts earlier numerical studies for silicene [33]. In any case, a temperature dependence with a pronounced maximum near or slightly below room temperature as displayed in Ref. [33] cannot be confirmed by our study.

In order to compare our results with experimental data, the 2D values in Fig. 6(a) for graphene have to be re-estimated to a corresponding 3D quantity dividing by the effective

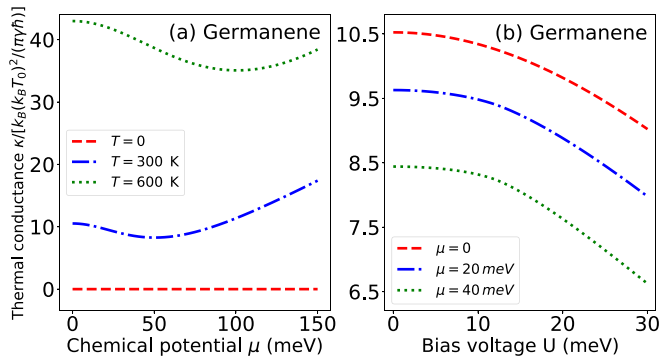


FIG. 7. Thermal conductance κ of germanene vs (a) chemical potential $|\mu|$ and (b) bias voltage $|U|$. In (a) the three curves correspond to the temperatures $T = 0$ (red-dashed), 300 (blue-dot-dashed), and 600 K (green-dot) and $U = 0$. In (b), three different occupation levels $|\mu| = 0$ (red-dotted), 20 (blue-dot-dashed), and 40 meV (green-dotted) are studied at room temperature.

graphene thickness $d = 3.35 \text{ \AA}$. This results approximately in a value of $\kappa/d = 1.13 \times \frac{100 \text{ meV}}{\gamma} \text{ W m}^{-1} \text{ K}^{-1}$ at room temperature and chemical potentials μ below 100 meV. Even for small broadening parameters of about 5 meV one finds electronic contributions to the in-plane thermal conductivity which are by two orders of magnitude smaller than experimental values of 2000–4000 $\text{W m}^{-1} \text{ K}^{-1}$ [62]. On the other hand, analytical studies including parameters for stanene suggest negligibility of the electronic part compared to the phonon thermal conductance only in the range below room temperature, whereas in the high-temperature range above 350 K the electronic contribution dominates [22].

The dependence of the thermal conductance κ on the doping level is displayed in Fig. 7(a). For vanishing $|\mu|$ the high-temperature limit (26) is generally realized. It shows a nonmonotonous, almost quadratic temperature behavior in agreement with studies for stanene [22]. For larger μ values, apart from almost vanishing κ values for $T = 0 \text{ K}$ (see Ref. [30]), a nonmonotonous variation of κ versus μ is visible. Thereby, the change of the absolute values remains small. With increasing chemical potential the κ values are first reduced. However, the curves at larger $|\mu|$ are closer to the opposite temperature limit (28). Similar tendencies are also visible in Fig. 7(b) by varying the effective spin-orbit coupling. The field modification of λ_{SO} to λ_{ξ_s} (2) by a finite U gives rise only to weak variation of the germanene properties expressed by a SOC constant of $\lambda_{\text{SO}} = 12 \text{ meV}$. Only for larger U values, i.e., large effective λ_{ξ_s} ones, κ is reduced as discussed in Fig. 6. The U dependence of κ is similar to that of σ in Fig. 5(b).

D. Conductance ratio

The Lorenz numbers $L = \kappa/(\sigma T)$ of the 2D carrier gases in graphene, silicene, germanene, stanene, and plumbene are plotted in Fig. 8 as a function of temperature. In units of $(k_B/e)^2$ we find an increase from about $\frac{\pi^2}{3} \sim 3.3$ at low temperatures, i.e., the Drude-Sommerfeld value, to values of approximately 7.8 at very high temperatures, more precisely for $|\mu| \ll k_B T$ and $|\lambda_{\text{SO}}| \ll k_B T$. Thereby, the influence of the Xene via the SOC constant λ_{SO} or the occupation level $|\mu|$ is

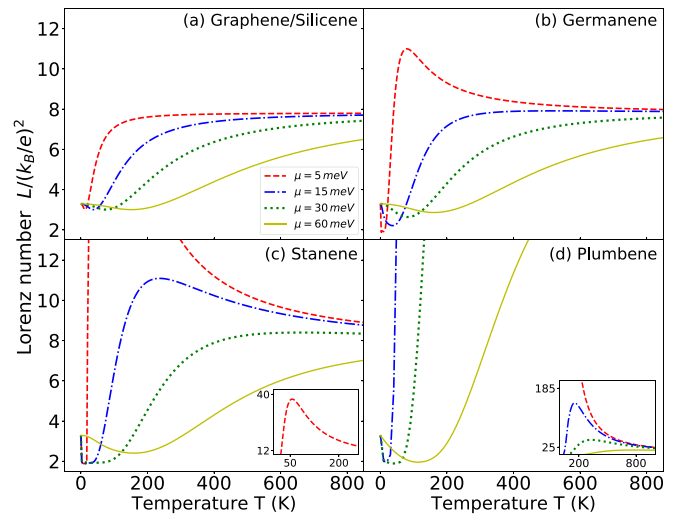


FIG. 8. Lorenz number L (18) in units of $(k_B/e)^2$ vs temperature T for (a) graphene/silicene, (b) germanene, (c) stanene, and (d) plumbene and four occupation levels $|\mu| = 5$ (red-dashed), 15 (blue-dot-dashed), 30 (green-dotted), and 60 meV (yellow-solid). The insets illustrate how the maxima of L for low occupation levels in the temperature interval somewhat below $T = 200$ (stanene) and 800 K (plumbene) depend on λ_{SO} .

seemingly more pronounced than in the cases σ and κ versus T . In all panels, after running through a minimum at extremely low temperatures, the Lorenz number tends to increase with rising temperature to values, which are higher by factors 2–3 than that of a classical 3D Drude gas. Nevertheless, in the low-temperature limit the L value of a Drude-Sommerfeld electron gas is reached. However, the shape of the curves L versus T significantly depends on the occupation level μ and the gap value $2\lambda_{\text{SO}}$. For a degenerate 2D carrier gas with the chemical potential μ in a conduction or valence band, $|\mu| > \lambda_{\text{SO}}$, and not too high temperatures all curves exhibit values $L < \pi^2/3(k_B/e)^2$ (28). The true increase toward $L = 6Li_3(-1)/Li_1(-1)(k_B/e)^2 \approx 7.804(k_B/e)^2$ (26) happens for all occupations at higher temperatures, approximately for $k_B T > |\mu|$. Dramatic changes happen for relatively large gaps, e.g., in germanene, stanene, and plumbene, and low doping $|\mu| < \lambda_{\text{SO}}$, i.e., in the case of classical carrier gases. The conductance ratio can exceed the limiting value of 7.804 in units of $(k_B/e)^2$. A pronounced maximum appears in the range of about 50–200 K, i.e., for $k_B T < \lambda_{\text{SO}}$.

The variations of the Lorenz number with the band occupation $|\mu|$ and the field modification of the spin-orbit coupling by the bias U are visible in Fig. 9. Figure 9(a) shows an unexpected behavior with a peak near $\mu = 0 \text{ meV}$, i.e., vanishing doping and the chemical potential in the middle of the gap of germanene. At the Dirac point, the low-temperature expansion breaks down and the details of the polylogarithmic functions become important [see (26)]. The absolute height and width of this peak are determined by the actual temperature. In addition, for lower temperatures the peak is accompanied by a dip below $L = \pi^2/3(k_B/e)^2$ (28) but converges with rising chemical potential in the conduction or valence bands to this value of L , behaving like graphene where $\lambda_{\text{SO}} = 0$ and μ is far from the Dirac point, i.e., $\mu \gg k_B T$. The effective coupling

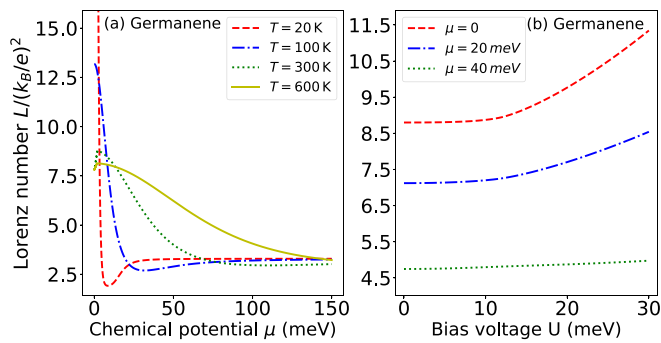


FIG. 9. Lorenz number L of germanene vs (a) chemical potential $|\mu|$ and (b) bias voltage $|U|$. In (a) the temperatures $T = 20$ (red-dashed), 100 (blue-dot-dashed), 300 (green-dotted), and 600 K (yellow-solid) are considered for $U = 0$. In (b), the three occupation levels $|\mu| = 0$ (red-dashed), 20 (blue-dot-dashed), and 40 meV (green-dotted) are studied at room temperature.

constants λ_{ξ_s} , fixed by U , hardly affect L . The influence of the variation of the effective SOC constant λ_{ξ_s} by a bias voltage U in Fig. 9(b) mainly indicates the suppression of the Lorenz number L at room temperature with rising μ . The topological transition of germanene from $U < \lambda_{SO}$ to $U > \lambda_{SO}$ [37] has only a minor influence, which is indicated by an increase of L for large bias voltages.

In general, the Wiedemann-Franz law $LT = \kappa/\sigma$ illustrates that the charged carriers of a system contribute to both the electrical transport and the heat transport and that the heat conductivity increases with temperature by a factor LT more than the electrical conductivity. Whereas in the majority of 3D metals [32] this increase is indeed linear with a constant Lorenz number L , the degenerate carrier gases in the 2D Xenon show a strong increase of L with rising temperature T with variations related to the fundamental gap and the doping level. This observed fact may be interpreted as a clear tendency that, above room temperature, the studied 2D crystals are better thermal conductors than 3D metals for a given electrical conductivity.

IV. SUMMARY AND CONCLUSIONS

Applying an electronic structure model including spin-orbit coupling, the electronic contributions to the heat capacity and thermal conductance are investigated by analytical and

numerical approaches. For comparison, also the electrical conductance is investigated. The electronic structure model is valid for low-energy Dirac-like excitations in the electron or hole gases in Xenon such as graphene, silicene, germanene, stanene, and plumbene. The scattering properties in the carrier gases, due to doping μ or temperature T , are modeled by a broadening parameter γ , which represents the reciprocal scattering time of the carriers, apart from the Planck's constant.

We derive analytical expressions for the heat capacity, the electrical conductance, the thermal conductance, and the Lorenz number in terms of incomplete Fermi-Dirac integrals. In the limit of vanishing spin-orbit coupling constants, i.e., in the graphene limit, analytical expressions in terms of complete Fermi-Dirac integrals or the polylogarithm functions are derived. The detailed behavior of the four studied quantities versus temperature and occupation level is discussed. This also holds for the material dependence via the SOC constant and the influence of the external bias U . The absolute values of the electron contributions to the thermal quantities, such as thermal conductance and Lorenz number are small compared to measured ones, at least for graphene, thus confirming that the phonon contribution is the dominant one. Very interesting is the resulting conductance ratio divided by the absolute temperature, the Lorenz number L . In contrast to what one knows from the classical or semiclassical electron gases in 3D, we observe special characteristics of the 2D Dirac fermion systems. At room or higher temperatures, depending on the actual values of λ_{SO} and μ , the L number converges to the high-temperature limit, which is larger by a factor 2–3 than that of a Drude-Sommerfeld gas. In general, it shows variations with temperature, occupation and material. Consequently, the thermal conductance in the 2D quantum materials does not follow the classical Wiedemann-Franz law, at least not at higher temperatures. This is especially a consequence of the band linearity around the Dirac point in wide ranges of the Brillouin zone around K or K' corner points.

ACKNOWLEDGMENTS

O.P. acknowledges financial funding from the EU MSCA-RISE project DiSeTCom (GA 823728) and from INFN project TIME2QUEST. CPU time was granted by CINECA and ENEA-CRESCO HPC centers.

- [1] F. Bechstedt, P. Gori, and O. Pulci, Beyond graphene: Clean, hydrogenated and halogenated silicene, germanene, stanene, and plumbene, *Prog. Surf. Sci.* **96**, 100615 (2021).
- [2] R. R. Nair, P. Blake, A. N. Grigorenko, K. S. Novoselov, T. J. Booth, T. Stauber, N. M. R. Peres, and A. K. Geim, Fine structure constant defines visual transparency of graphene, *Science* **320**, 1308 (2008).
- [3] Y. Zhang, Y.-W. Tan, H. L. Stormer, and P. Kim, Experimental observation of the quantum Hall effect and Berry's phase in graphene, *Nature (London)* **438**, 201 (2005).
- [4] S. V. Morozov, K. S. Novoselov, M. I. Katsnelson, F. Schedin, D. C. Elias, J. A. Jaszczak, and A. K. Geim, Giant Intrinsic

Carrier Mobilities in Graphene and Its Bilayer, *Phys. Rev. Lett.* **100**, 016602 (2008).

- [5] A. Balandin, S. Ghosh, W. Bao, I. Calizo, D. Teweldebrhan, F. Miao, and C. Ning Lau, Superior thermal conductivity of single-layer graphene, *Nano Lett.* **8**, 902 (2008).
- [6] E. Scalise, M. Houssa, G. Pourtois, B. van den Broek, V. Afanasev, and A. Stesmans, Vibrational properties of silicene and germanene, *Nano Res.* **6**, 19 (2013).
- [7] L. Matthes, O. Pulci, and F. Bechstedt, Massive Dirac quasiparticles in the optical absorbance of graphene, silicene, germanene, and tinene, *J. Phys.: Condens. Matter* **25**, 395305 (2013).

- [8] L. Matthes, P. Gori, O. Pulci, and F. Bechstedt, Universal infrared absorbance of two-dimensional honeycomb group-IV crystals, *Phys. Rev. B* **87**, 035438 (2013).
- [9] X.-L. Wang, S. Dou, and C. Zhang, Zero-gap materials for future spintronics, electronics and optics, *NPG Asia Mater.* **2**, 31 (2010).
- [10] Y. Ohtsubo, P. Le Fèvre, F. M. C. Bertran, and A. Taleb-Ibrahimi, Dirac Cone with Helical Spin Polarization in Ultrathin α -Sn(001) Films, *Phys. Rev. Lett.* **111**, 216401 (2013).
- [11] Y. Xu, Z. Gan, and S.-C. Zhang, Enhanced Thermoelectric Performance and Anomalous Seebeck Effects in Topological Insulators, *Phys. Rev. Lett.* **112**, 226801 (2014).
- [12] C.-C. Liu, W. Feng, and Y. Yao, Quantum Spin Hall Effect in Silicene and Two-Dimensional Germanium, *Phys. Rev. Lett.* **107**, 076802 (2011).
- [13] Y. Xu, B. Yan, H.-J. Zhang, J. Wang, G. Xu, P. Tang, W. Duan, and S.-C. Zhang, Large-Gap Quantum Spin Hall Insulators in Tin Films, *Phys. Rev. Lett.* **111**, 136804 (2013).
- [14] L. Matthes, S. Küfner, J. Furthmüller, and F. Bechstedt, Quantization and topological states in the spin Hall conductivity of low-dimensional systems: An *ab initio* study, *Phys. Rev. B* **93**, 121106(R) (2016).
- [15] F. Matusalem, M. Marques, L. K. Teles, L. Matthes, J. Furthmüller, and F. Bechstedt, Quantization of spin Hall conductivity in two-dimensional topological insulators versus symmetry and spin-orbit interaction, *Phys. Rev. B* **100**, 245430 (2019).
- [16] X.-L. Yu and J. Wu, Evolution of the topological properties of two-dimensional group IVA materials and device design, *Phys. Chem. Chem. Phys.* **20**, 2296 (2018).
- [17] N. Li, J. Ren, L. Wang, G. Zhang, P. Hänggi, and B. Li, Colloquium: Phononics: Manipulating heat flow with electronic analogs and beyond, *Rev. Mod. Phys.* **84**, 1045 (2012).
- [18] A. Balandin, Thermal properties of graphene and nanostructured carbon materials, *Nat. Mater.* **10**, 569 (2011).
- [19] H. Xie, M. Hu, and H. Bao, Thermal conductivity of silicene from first-principles, *Appl. Phys. Lett.* **104**, 131906 (2014).
- [20] P. Gori, O. Pulci, R. de Lieto Vollaro, and C. Guattari, Thermophysical properties of the novel 2D materials graphene and silicene: Insights from *ab initio* calculations, *Energy Procedia* **45**, 512 (2014).
- [21] Y. Han, J. Dong, Q. G., and M. Hu, Phonon transport in the ground state of two-dimensional silicon and germanium, *RSC Adv.* **6**, 69956 (2016).
- [22] H. Zhou, Y. Cai, G. Zhang, and Y.-W. Zhang, Quantum thermal transport in stanene, *Phys. Rev. B* **94**, 045423 (2016).
- [23] L. Zhang, H. Zhao, W.-X. Ji, C.-W. Zhang, P. Li, and P.-J. Wang, Discovery of a new quantum spin Hall phase in bilayer plumbene, *Chem. Phys. Lett.* **712**, 78 (2018).
- [24] S. Mahdavi, S. F. Shayesteh, and M. B. Tagani, Electronic and mechanical properties of Plumbene monolayer: A first-principle study, *Physica E* **134**, 114837 (2021).
- [25] H. Li and R. Zhang, Vacancy-defect-induced diminution of thermal conductivity in silicene, *Europhys. Lett.* **99**, 36001 (2012).
- [26] M. Hu, X. Zhang, and D. Poulikakos, Anomalous thermal response of silicene to uniaxial stretching, *Phys. Rev. B* **87**, 195417 (2013).
- [27] Q.-X. Pei, Y.-W. Zhang, Z.-D. Sha, and V. Shenoy, Tuning the thermal conductivity of silicene with tensile strain and isotopic doping: A molecular dynamics study, *J. Appl. Phys.* **114**, 033526 (2013).
- [28] X. Zhang, H. Xie, M. Hu, H. Bao, S. Yue, G. Qin, and G. Su, Thermal conductivity of silicene calculated using an optimized Stillinger-Weber potential, *Phys. Rev. B* **89**, 054310 (2014).
- [29] E. Muñoz, J. Lu, and B. I. Yakobson, Ballistic thermal conductance of graphene ribbons, *Nano Lett.* **10**, 1652 (2010).
- [30] D. Nika and A. Balandin, Two-dimensional phonon transport in graphene, *J. Phys.: Condens. Matter* **24**, 233203 (2012).
- [31] M. Gadeghi, M. Pettes, and L. Shi, Thermal transport in graphene, *Solid State Commun.* **152**, 1321 (2012).
- [32] N. W. Ashcroft and N. D. Mermin, *Solid State Physics* (Saunders College, Philadelphia, 1976).
- [33] A. Feyzi and R. Chegel, Heat capacity, electrical and thermal conductivity of silicene, *Eur. Phys. J. B* **89**, 193 (2016).
- [34] R. Chegel and S. Behzad, Tunable electronic, optical, and thermal properties of two-dimensional germanene via an external electric field, *Sci. Rep.* **10**, 704 (2020).
- [35] C.-C. Liu, H. Jiang, and Y. Yao, Low-energy effective Hamiltonian involving spin-orbit coupling in silicene and two-dimensional germanium and tin, *Phys. Rev. B* **84**, 195430 (2011).
- [36] M. Ezawa, A topological insulator and helical zero mode in silicene under an inhomogeneous electric field, *New J. Phys.* **14**, 033003 (2012).
- [37] L. Matthes and F. Bechstedt, Influence of edge and field effects on topological states of germanene nanoribbons from self-consistent calculations, *Phys. Rev. B* **90**, 165431 (2014).
- [38] L. Stille, C. J. Tabert, and E. J. Nicol, Optical signatures of the tunable band gap and valley-spin coupling in silicene, *Phys. Rev. B* **86**, 195405 (2012).
- [39] C. Kittel, *Introduction to Solid State Physics*, 8th ed. (Wiley, New York, Chichester, 2005).
- [40] H. Mousavi and J. Khodadadi, Electronic heat capacity and thermal conductivity of armchair graphene nanoribbons, *Appl. Phys. A* **122**, 14 (2016).
- [41] M. Jonson and G. D. Mahan, Mott's formula for the thermopower and the Wiedemann-Franz law, *Phys. Rev. B* **21**, 4223 (1980).
- [42] I. Paul and G. Kotliar, Thermal transport for many-body tight-binding models, *Phys. Rev. B* **67**, 115131 (2003).
- [43] A. V. Joura, D. O. Demchenko, and J. K. Freericks, Thermal transport in the Falicov-Kimball model on a Bethe lattice, *Phys. Rev. B* **69**, 165105 (2004).
- [44] M. Jonson and G. D. Mahan, Electron-phonon contribution to the thermopower of metals, *Phys. Rev. B* **42**, 9350 (1990).
- [45] G. Grosso and G. Pastori Parravicini, *Solid State Physics* (Academic Press, San Diego, 2000).
- [46] N. M. R. Peres, J. M. B. Lopes dos Santos, and T. Stauber, Phenomenological study of the electronic transport coefficients of graphene, *Phys. Rev. B* **76**, 073412 (2007).
- [47] T. Stauber, N. M. R. Peres, and F. Guinea, Electronic transport in graphene: A semiclassical approach including midgap states, *Phys. Rev. B* **76**, 205423 (2007).
- [48] D. K. Efetov and P. Kim, Controlling Electron-Phonon Interactions in Graphene at Ultrahigh Carrier Densities, *Phys. Rev. Lett.* **105**, 256805 (2010).

- [49] E. Muñoz, Phonon-limited transport coefficients in extrinsic graphene, *J. Phys.: Condens. Matter* **24**, 195302 (2012).
- [50] X. He, F. Lin, F. Liu, and H. Zhang, Investigation of phonon scattering on the tunable mechanisms of terahertz graphene metamaterials, *Nanomaterials* **10**, 39 (2020).
- [51] Z. Wang, T. Feng, and X. Ruan, Thermal conductivity and spectral phonon properties of freestanding and supported silicene, *J. Appl. Phys.* **117**, 084317 (2015).
- [52] N. Gupta, and R. Verma, Thermoelectric performance of silicene under uniform biaxial strain: A first principles study, *Superlattices Microstruct.* **156**, 106944 (2021).
- [53] A. Mazloom, F. Parhizgar, S. H. Abedinpour, and R. Asgari, Relaxation times and charge conductivity of silicene, *Phys. Rev. B* **94**, 035153 (2016).
- [54] L. Matthes, S. Küfner, J. Furthmüller, and F. Bechstedt, Intrinsic spin Hall conductivity in one-, two-, and three-dimensional trivial and topological systems, *Phys. Rev. B* **94**, 085410 (2016).
- [55] G. D. Mahan, *Many-Particle Physics*, 2nd ed. (Plenum Press, New York, 1990).
- [56] M. Lee, Polylogarithmic analysis of chemical potential and fluctuations in a D-dimensional free Fermi gas at low temperatures, *J. Math. Phys.* **36**, 1217 (1995).
- [57] L. Lewin, *Dilogarithms and Associated Functions* (McDonald, London, 1958).
- [58] H. Mousavi and J. Khodadadi, Electronic heat capacity and conductivity of gapped graphene, *Physica E* **150**, 11 (2013).
- [59] M. Abramowitz and I. Stegun, *Handbook of Mathematical Functions* (Dover Publications, New York, 1964).
- [60] U. Wurstbauer, C. Röling, U. Wurstbauer, W. Wegscheider, M. Vaupel, P. H. Thiesen, and D. Weiss, Imaging ellipsometry of graphene, *Appl. Phys. Lett.* **97**, 231901 (2010).
- [61] K. S. Novoselov, A. K. Geim, S. V. Morozov, D. Jiang, Y. Zhang, S. V. Dubonos, I. V. Grigorieva, and A. A. Firsov, Electric field effect in atomically thin carbon films, *Science* **306**, 666 (2004).
- [62] E. Pop, V. Varshney, and A. Roy, Thermal properties of graphene: Fundamentals and applications, *MRS Bull.* **37**, 1273 (2012).
- [63] L. Benedict, S. Louie, and M. Cohen, Heat capacity of carbon nanotubes, *Solid State Commun.* **100**, 177 (1996).
- [64] S. Zaveh, M. Roknabadi, T. Morshedloo, and M. Modarresi, Electronic and thermal properties of germanene and stanene by first-principles calculations, *Superlattices Microstruct.* **91**, 383 (2016).
- [65] S. Trivedi, A. Srivastava, and R. Kurchania, Silicene and germanene: A first principle study of electronic structure and effect of hydrogenation-passivation, *J. Comput. Theor. Nanosci.* **11**, 781 (2014).
- [66] A. Mogulkoc, M. Modarresi, B. Kandemir, and M. Roknabadi, Magnetotransport properties of corrugated stanene in the presence of electric modulation and tilted magnetic field, *Phys. Status Solidi B* **253**, 300 (2016).
- [67] D. Grassano, O. Pulci, V. O. Shubnyi, S. G. Sharapov, V. P. Gusynin, A. V. Kavokin, and A. A. Varlamov, Detection of topological phase transitions through entropy measurements: The case of germanene, *Phys. Rev. B* **97**, 205442 (2018).
- [68] K. Bolotin, K. Sikes, Z. Jiang, M. Klima, G. Fudenberg, J. Hone, P. Kim, and H. Stormer, Ultrahigh electron mobility in suspended graphene, *Solid State Commun.* **146**, 351 (2008).
- [69] P. Ledwith, W. J. M. Kort-Kamp, and D. A. R. Dalvit, Topological phase transitions and quantum Hall effect in the graphene family, *Phys. Rev. B* **97**, 165426 (2018).